PAPER

Check for updates

Disentangling the molecular polarizability and first hyperpolarizability of methanol–air interfaces†

Tárcius N. Ramos (ID) * and Benoît Champagne (ID)

Liquid–air interfaces have extensive implications in different areas of interest because the dynamical processes at the interface can be different from those in bulk. Thus, its characterization, understanding, and control may be pivotal in advancing discoveries. However, characterizing the interface requires special and selective tools to avoid signals from the bulk region. This surface specificity and versatility is achieved by using the second harmonic generation (SHG) responses. This study adopts multiscale simulation methods to evaluate the surface SHG responses of methanol–air interfaces with submonolayer resolution tackled by sequentially using classical molecular dynamics simulations under different temperatures and then employing quantum chemistry methods to compute the molecular first hyperpolarizabilities (β). This approach ensures the configurational diversity required to evaluate the average β values. The main achievements are (i) a quasi-absence of surface sensitivity of the mean polarizability $\langle \alpha \rangle$ with values about 2% larger than those obtained in bulk, (ii) conversely, smooth variations on the polarizability anisotropy $\Delta\alpha$ are observed up to the fourth molecular layer at around 20 Å from the interface, and (iii) narrow interfacial effects on the SHG responses, $\beta(-2\omega;\omega,\omega)$, which are limited to the first molecular layer (~ 3.0 Å) and characterized by a high contrast in the $\beta_{ZZZ}(-2\omega;\omega,\omega)$ tensor component between the first and the subsequent layers. Similar trends are obtained at different temperatures or when increasing the number of methanol molecules treated at the quantum chemistry level, indicating the robustness of the approach for describing the dipolar molecular responses of air–liquid interfaces.

1. Introduction

Dynamic processes at liquid–air interfaces have extensive implications in a broad area of applications like catalysis, electrochemistry, and environmental science.[1,2] Understanding and characterizing these interfacial phenomena is of paramount importance, as they may play a pivotal role in advancing discoveries. Notably, the interfacial water region exhibits larger reaction rate constants compared to the bulk phase, making it crucial in life sciences.[2] However, optically probing these interfaces is challenging because the bulk signals often dominate the light–matter interaction responses, and surface-specific techniques are required to characterize these regions. The second harmonic generation (SHG) technique is a powerful optical tool to probe interfaces due to its surface specificity, versatility, and

simplicity.[3] SHG is a second-order nonlinear optical (NLO) phenomenon, which converts pairs of photons of $\hbar\omega$ energy into photons of $2\hbar\omega$ energy. Its surface specificity, under the electric–dipole approximation, is related to the forbidden responses of media with inversion symmetry.[4] Historically, the theory of surface SHG was formulated in 1962 by Bloembergen and Pershan,[5] who extended the Maxwell's equations at the boundary of nonlinear media, one year after the first experimental observations of SHG.[6] Since its formulation and owing to the development of controlled laser beams and more sensitive detectors,[1–4,7–11] surface SHG has attracted much attention and has led to successful applications in a broad range of surface science disciplines.

From the modeling point of view, the SHG responses of dynamical systems are calculated using a multiscale sequential approach,[12] where (i) thermodynamically accessible structures are first produced using molecular dynamics (MD) simulations to probe the structural diversity and where (ii) the NLO responses are then evaluated using quantum chemistry (QC) methods. Similar approaches have also been applied to interfaces, where snapshots extracted from MD simulations have been used for calculating the SHG of lipid bilayers,[13,14] functionalized materials,[15,16] and liquid–air and liquid–liquid interfaces as well.[17–20] An important aspect to tackle with these

---

Theoretical Chemistry Lab, Unit of Theoretical and Structural Physical Chemistry, Namur Institute of Structured Matter, University of Namur, rue de Bruxelles, 61, B-5000 Namur, Belgium. E-mail: tarcius.nascimento@unamur.be

8658 | *Phys. Chem. Chem. Phys.*, 2024, **26**, 8658–8669

This journal is © the Owner Societies 2024

methods is the relationship between the microscopic first hyperpolarizability (β, a rank-3 tensor) and the corresponding macroscopic second-order NLO susceptibility ($\chi^{(2)}$, a similar rank-3 tensor) of the interfaces. This relationship depends on orientational averages and is well-established for adsorbed molecules at interfaces.[21] However, this is less the case for pure liquids, in which different assumptions of the averaging procedure lead to different results,[19] and a consensus has not yet been reached to take into account the effects of intermolecular interactions. In general (for interfaces), the transformation from the microscopic to macroscopic responses has been performed by using the average orientational profile (from MD simulations) of the β tensor (determined at a given QC level) around the surface normal direction. This approach usually predicts NLO active regions beyond the first molecular layer thickness due to the interface roughness incorporated in the average orientational profile. Moreover, like pure liquids, whether the scattering units are individual molecules or clusters of molecules remains an open question. Indeed, the impact of the hyperpolarizability fluctuations has been observed in bulk liquid water,[22] and this should also play a role at the interfaces.

The current study adopts multiscale simulation methods to evaluate the "microscopic" surface SHG responses of methanol–air interfaces. The submonolayer resolution of the surface SHG response is tackled by sequentially using classical MD simulations under different temperatures and then employing QC methods to compute the molecular first hyperpolarizabilities. In the later step, an increasing number of molecules is treated at the QC level and a decomposition scheme is employed. Moreover, identification and indexation of each molecule as belonging to a given molecular layer allows to disentangle the contribution of the first layers from those of the other layers and to capture a surface SHG monolayer resolution. Besides considering another liquid, this approach represents a step forward compared to our previous study on the water–air interface[20] by including the temperature effects, the dependence on the number of molecules in the QC region, and analyses of property decomposition. In addition, it represents a step toward experimental results obtained for *n*-alcohols.[23]

This paper is organized as follows: a brief description of the NLO responses is presented and is followed by the details of the employed computational methods in the Methodology section. Next, the results and discussions are divided into reference bulk calculations and interfacial effects. The conclusions are finally drawn in the last section.

2. Methodology

2.1 Basics of nonlinear optical responses

Oscillating electric fields [$\vec{E}^{\omega}$] interacting with matter give rise to induced dipole moments [$\Delta\vec{\mu}(\omega_\sigma)$], which are expressed in the form of Taylor expansions [T convention, eqn (1)]. The electric field perturbations on the molecular electronic structures are described by their "microscopic" properties associated with the linear response termed polarizability (α, a rank-2 tensor), and the

nonlinear ones termed the first hyperpolarizability (β, a rank-3 tensor), the second hyperpolarizability (γ, a rank-4 tensor), and so on.

$$
\begin{aligned}
\Delta\mu_i(\omega_\sigma) =\ & \sum_j \alpha_{ij}(-\omega_\sigma; \omega_1)E_j^{\omega_1} \\
& + \frac{1}{2}\sum_{j,k} \beta_{ijk}(-\omega_\sigma; \omega_1, \omega_2)E_j^{\omega_1} E_k^{\omega_2} \\
& + \frac{1}{6}\sum_{j,k,l} \gamma_{ijkl}(-\omega_\sigma; \omega_1, \omega_2, \omega_3)E_j^{\omega_1} E_k^{\omega_2} E_l^{\omega_3} \\
& + \cdots,
\end{aligned} \tag{1}
$$

where $\omega_\sigma = \sum_n \omega_n$ is the response angular frequency due to the perturbations.[24]

Several invariants are associated with the various macroscopic or observable properties. These are obtained from combining the tensor components. Here, the focus is on the so-called mean [$\langle\alpha\rangle$, eqn (2)] and anisotropic [$\Delta\alpha$, eqn (3)] polarizability, and on the Hyper–Rayleigh Scattering (HRS)[25] first hyperpolarizability [β_{HRS}, eqn (4)] and its corresponding depolarization ratio [DR, eqn (5)]. The HRS experiment probes the incoherent responses by analyzing the intensities of the vertically-polarized (along Z) scattered light, which is usually collected at 90° angle with respect to the incident beam.[25] The $\langle\beta_{ZZZ}^2\rangle$ response [eqn (6)] corresponds to the intensity obtained for a vertically-polarized incident light, whereas the $\langle\beta_{ZXX}^2\rangle$ response [eqn (7)] to the horizontally-polarized (along X) incident light.[26] The lower-case indices [*e.g.*, eqn (1)] define the molecular axes coordinates while the upper-case [*e.g.*, eqn (4)] define the laboratory axes. The HRS technique was developed to measure the first hyperpolarizability of molecules in solutions, and, in our analysis, it is employed to monitor the variation of the SHG responses as well as the modification of "symmetry" effects between the bulk and interfacial regions. Additionally, the Cartesian components of the vectorial representation of β are given in eqn (8). This quantity is relevant for describing the $\beta_\parallel$ response [eqn (9)], the $\vec{\beta}$ projection onto $\vec{\mu}$, which is associated with the electric field induced SHG (EFISHG) response. $\theta_{(\mu,\beta)}$ is the angle between $\vec{\mu}$ and $\vec{\beta}$.

$$
\langle\alpha\rangle = \frac{1}{3}\sum_i \alpha_{ii} \tag{2}
$$

$$
\Delta\alpha = \sqrt{\frac{1}{2}\sum_{ij}\left(3\alpha_{ij}^2 - \alpha_{ii}\alpha_{jj}\right)} \tag{3}
$$

$$
\beta_{HRS} = \sqrt{\langle\beta_{ZZZ}^2\rangle + \langle\beta_{ZXX}^2\rangle} \tag{4}
$$

$$
DR = \frac{\langle\beta_{ZZZ}^2\rangle}{\langle\beta_{ZXX}^2\rangle} \tag{5}
$$

$$
\langle\beta_{ZZZ}^2\rangle = \frac{1}{105}\sum_{ijk}\left[\begin{array}{c} 2\beta_{ijk}^2 + \beta_{iij}\beta_{ikk} \\ +4\left(\beta_{iij}\beta_{jkk} + \beta_{iij}\beta_{kkj} + \beta_{ijk}\beta_{jik}\right)\end{array}\right] \tag{6}
$$

This journal is © the Owner Societies 2024

Phys. Chem. Chem. Phys., 2024, **26**, 8658–8669 | **8659**

$$\langle \beta_{ZXX}^2 \rangle = \frac{1}{105} \sum_{ijk} \begin{bmatrix} 6\beta_{ijk}^2 + 3\beta_{ijj}\beta_{ikk} \\ -2(\beta_{iij}\beta_{jkk} + \beta_{iij}\beta_{kkj} + \beta_{ijk}\beta_{jik}) \end{bmatrix} \quad (7)$$

$$\beta_i = \frac{1}{3} \sum_j (\beta_{ijj} + \beta_{jij} + \beta_{jji}) \quad (8)$$

$$\beta_{\parallel} = \frac{3}{5} |\vec{\beta}| \cos(\theta_{(\mu,\beta)}) \quad (9)$$

2.2 Molecular dynamic simulations

MD simulations were performed to sample energetically allowed configurations in the liquid phase. A cubic box was filled with 5000 methanol (MeOH) molecules, assuming a 0.8 g cm^{-3} density, resulting in a box edge of L = 69.3 Å. The MeOH molecules were represented by the OPLS-AA force field[27] (in a.u.: q_O = −0.683, q_{HO} = 0.418, q_C = 0.145, q_{HC} = 0.040). Following a standard procedure, the atomic positions were first relaxed to minimize the potential energy of the initial structure using the steepest descent algorithm with a 350 kJ mol^{-1} nm^{-1} force tolerance criterium; second, the thermalization was performed in two steps. First, the dynamics was run for 2.5 ns within the NVT ensemble (at T = 300 K) and then for additional 2.5 ns within the NPT ensemble (P = 1 atm) at three temperatures (260, 280, and 300 K). Last, extra 30 ns of trajectories were created as the production step for each temperature within the NPT ensemble. The considered range of temperatures is far from the $\sim$175 K freezing point,[28] ensuring the liquid phase of the MeOH. These MD simulations provide structures of the bulk MeOH phase. To simulate the interfaces, the Z-edge of the cubic boxes was then extended to 300 Å, creating a vacuum of about 230 Å between the two interfaces and ensuring slab conditions. The MeOH–air interface simulations were performed within the NVT ensemble for 30 ns.

All the MD simulations were performed using the leap-frog integrator[29] with a 1 fs time step. The short-range interactions were accounted for up to 14 Å distance, and long-range electrostatic corrections were incorporated by the smooth Particle–Mesh Ewald method.[30] The Berendsen thermostat[31] and barostat[32] were coupled every 0.1 and 1.0 ps, respectively. The hydrogen bonds were constrained using the LINCS algorithm.[33] All MD simulations were carried out on GROMACS.[34,35] Snapshots of the bulk and slab simulation boxes are presented in Fig. 1.

2.3 Classical trajectories analyses

Radial distribution functions (RDFs) are used to examine how the density of particles varies as a function of the distance between pairs of atoms. Its structures provide the average size of the coordination shells as well as the associated coordination numbers after integrating it.

Hydrogen bond analysis is a helpful tool for understanding the intermolecular interactions. Geometrical criteria were used to assess these values. A hydrogen bond (H-bond) is assigned when the donor–acceptor distance is smaller than 3.5 Å and the donor–hydrogen–acceptor angle is larger than 140°. Layer-selective H-bond values were computed using the molecular
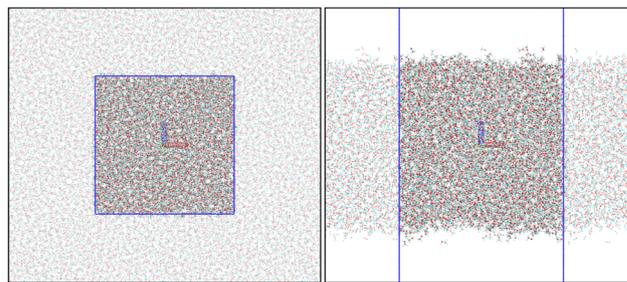

Fig. 1 Snapshots from bulk (left) and slab (right) MD simulations. The blue lines identify the MD simulation boxes. The images were created using VMD.[36]

layer index (described below) for disentangling the intralayer and interlayer interactions.

The static dielectric constant (ϵ_r) of the bulk phase was computed as an extra parameter to assess the accuracy of the molecular force field for describing the electrostatic environmental effects since they play a key role in modulating the NLO properties. ϵ_r [eqn (10)] was estimated using the fluctuation of the dipole moment vector of the whole simulation box [$\vec{M}$, eqn (11)], comprising N molecules within a V volume and under a T temperature following the expressions derived by Neumann.[37] The computations were carried out using the MDAnalysis[38] Python package.

$$\epsilon_r = 1 + \frac{4\pi}{V} \frac{1}{3k_b T} \sum_{i=x,y,z} \left(\langle M_i^2 \rangle - \langle M_i \rangle^2 \right) \quad (10)$$

$$\vec{M} = \sum_n^N \vec{\mu}_n. \quad (11)$$

The interfacial density profile [$\rho(Z)$] along the direction of the normal to the interface describes a sigmoid function [eqn (12)] relating the density of the bulk-like region (ρ_{center}, termed as center, not to be confused with the bulk properties coming from the bulk reference MD simulations), the z-coordinate defining the interface position (z_0 corresponds to $\rho(z_0) = \rho_{center}/2$), and the interfacial thickness (D) corresponding to density change from 90% to 10%, which reflects the roughness of the interface.[2]

$$\rho(z) = \frac{\rho_{center}}{2} \left(1 - \tanh \frac{z - z_0}{D} \right) \quad (12)$$

Molecular layers were defined by moving probe spheres of 1.5 Å radius from top to bottom inside the simulation boxes. Starting from above the interface, these probe spheres stop their movement when touching an atom, assigning it as belonging to the first molecular layer. After defining the molecules of the first molecular layer, they are removed and the probe movement resumes to define the second, third, and following molecular layers. The possible evaporated molecules are excluded from this procedure by a neighbor minimum distance criterion of 3.5 Å. This procedure is known as identification of the truly interfacial molecules (ITIM)[39] and was performed using the Pytim[40] package. Since the molecules are

8660 | Phys. Chem. Chem. Phys., 2024, 26, 8658–8669

This journal is © the Owner Societies 2024

indexed as belonging to a given molecular layer through the whole trajectory, it becomes straightforward to compute their density profiles and the intralayer and interlayer properties, as well as to extract molecular clusters for the NLO computations.

2.4 Quantum chemistry calculations

Time-dependent density functional theory (TD-DFT) was employed in its linear and quadratic formalisms[41] to compute the polarizabilities and first hyperpolarizabilities. Based on our previous results in describing the NLO properties of interfacial water molecules,[20] the CAM-B3LYP[42] exchange–correlation (XC) functional and the aug-cc-pVDZ[43] basis set were used in the current study. In ref. 20, B3LYP and CAM-B3LYP XC functionals provided the same trends, while the aug-cc-pVDZ basis set gave a good compromise between CPU time and accuracy in comparison to aug-cc-pVTZ. Also, CAM-B3LYP has been reported to deliver good accuracy in simulating the NLO properties of small molecules.[44] The environment effects were accounted for using the polarizable embedding (PE)[45] approach and including the external effective field[46] for the solvent embedding potential derived for MeOH[47] (in a.u.: $q_O = -0.59543$, $q_{HO} = 0.38068$, $q_C = 0.18382$, $q_{HC} = 0.01031$, $\alpha_O = 5.60297$, $\alpha_{HO} = 1.85100$, $\alpha_C = 6.42738$, $\alpha_{HC} = 2.50587$). All calculations were performed with the Dalton software[48,49] considering the frequently employed optical perturbation at 1064 nm wavelength.

Additionally, the convergence of the optical properties as a function of the embedding size was investigated for both the bulk and the interface, with a QC region comprising only one MeOH molecule. These embeddings were spherical with a radius ranging from 15 Å to 30 Å, either considering a shell of charges and polarizabilities centered at the atoms or also, in addition, a second external shell of only point charges. All the NLO results reported in the following sections were obtained for a cluster encompassing N MeOH molecules (N = 1, 3, and 6) surrounded by 20 Å of polarizable and point charge sites. The left side of Fig. 2 shows a representative snapshot illustrating the interface model including the quantum region with N = 6 and the 20 Å embedding, while its right side shows a detailed picture of the cluster highlighting the central (vdW representation), the hydrogen-bonded (blue), and the first neighboring (orange) MeOH molecules.
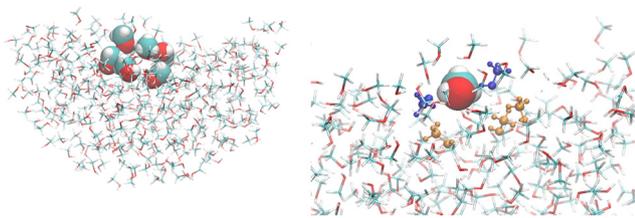

Fig. 2 A snapshot illustrating the interfacial model used in the quantum chemical calculations. Left: A cluster with 6 MeOH molecules surrounded by 20 Å of polarizable embedding sites. Right: A detailed view of the cluster highlighting the central (vdW representation), the hydrogen-bonded (blue), and first neighbors (orange) MeOH molecules. The images were created using VMD.[36]

2.5 Decomposition into local properties

Partitioning the molecular properties could also help understanding its properties as a function of its constituents. It becomes more relevant when this decomposition is performed on extended systems, large molecules, or clusters of small molecules. Here, the local properties (LoProp) approach[50] was employed to separate the β contribution of each MeOH molecule belonging to the quantum region. It allows to understand the impact of the hydrogen bonds and of the first neighbors on the first hyperpolarizability and to unravel how they affect the SHG interfacial signal. The dynamic β response decomposition is obtained by projecting the second-order electronic density perturbation into atomic basis functions, providing the β contribution of each atom. Therefore, the β response of each MeOH molecule of a cluster is obtained by summing its atomic contributions. These calculations were performed using the "LoProp for Dalton" program.[51]

3. Results and discussions

3.1 Structural analysis

3.1.1 Bulk MeOH. The RDFs of the oxygen [$g(r)_{OO}$], carbon [$g(r)_{CC}$], and center-of-mass [$g(r)_{COM-COM}$] are shown in Fig. S1–S3 (ESI†) for T = 260, 280, and 300 K. Since this 40 K temperature range is far from phase transitions, similar distributions are observed at different temperatures. The first peak of $g(r)_{OO}$ $\sim$ 2.8 Å is related to the hydrogen-bond shell, and it provides a coordination number of 2 MeOH molecules at the first valley (at 3.5 Å). This is in agreement with what has been observed using X-ray diffraction ($g(r)_{OO}$ peaks at 2.7 Å)[52] and more recently using extended X-ray absorption fine structure (EXAFS) in liquid microjets ($g(r)_{OO}$ peaks at $\sim$2.75 Å).[53] The $g(r)_{OO}$ distributions also show two additional peaks after the hydrogen-bond shell before smoothly converging at 10 Å. The structure defining the "first" solvation shell shows its maximum at 4.75 Å and its minimum at 6.10 Å (except for T = 300 K, where it is 6.15 Å), which are associated with coordination numbers of 5 and 14 MeOH molecules. In a consistent way, the CC distributions present three peaks, the $g(r)_{COM-COM}$ distribution is even better suited for analyzing the MeOH solvation shells. Four well-defined peaks describe successively the hydrogen bonds and the following solvation shells of MeOH in the bulk region. Its coordination number corroborates that 2 surrounding MeOH molecules interact *via* H-bonds with the central MeOH. Then, the peak of the first solvation shell ($\sim$4.5 Å) encompasses 5 molecules, and its valley around 6.2 Å encompasses 14 MeOH molecules. From these results, the following numbers of MeOH molecules included in the QC region for the calculations of the NLO responses are defined: N = 1 (only the central molecule), N = 3 (the central molecule and its H-bonded molecules), and N = 6 (the central molecule and the 5 nearest defining the first solvation shell are also included). The average numbers of H-bond interacting MeOH were determined from the entire trajectory by considering the following geometrical criteria: (i) oxygen–oxygen donor–acceptor distance $d_{DA} \leq 3.5$ Å and (ii) donor–hydrogen–acceptor angle $\theta_{DHA} \geq 140.0°$. The

This journal is © the Owner Societies 2024

Phys. Chem. Chem. Phys., 2024, **26**, 8658–8669 | **8661**

Table 1 Temperature dependence of the density, of the average number of hydrogen bonds, and of the dielectric constant of MeOH simulated in bulk

T [K]	ρ [g cm^{-3}]	# H-Bonds	ϵ_r OPLS-AA	ϵ_r PE
260	0.816	1.89	32.79	35.98
280	0.794	1.84	29.97	32.72
300	0.771	1.78	25.74	27.81

values show a decrease with the temperature (from 1.89 to 1.78, Table 1) as expected due to the decrease of the density (from 0.816 to 0.771 g cm^{-1}, Table 1). Moreover, the values match the coordination numbers associated with the H-bond peaks of $g(r)_{OO}$. These results provide trustworthy dynamical structures to be used in subsequent calculations of their linear and nonlinear optical properties.

Table 1 also lists the dielectric constants [ϵ_r, eqn (10)], which decreases from ~ 33 (at $T = 260$ K) to ~ 26 (at $T = 300$ K) when increasing the temperature, presenting the same trend as that observed in experiments [36.88 ($T = 278.15$ K), 35.40 ($T = 283.15$ K), 33.30 ($T = 293.15$ K), 32.66 ($T = 298.15$ K), and 31.69 ($T = 303.15$ K)].[54,55] One reason for this reasonable agreement between the theoretical results derived using the OPLS-AA charges originates from the fact that this force field has been designed to reproduce macroscopic properties associated with the potential energy surface.[56] However, the dielectric constant depends also on the dipole moment surface of the system, that is, how the dipole moment of the system changes as a function of the nuclei coordinates. In terms of absolute values, classical non-polarizable force fields lack induction effects when predicting dielectric constants, and an empirical scaling factor of 1.26 usually leads to a better theoretical–experimental match.[56] Applying this scaling factor modifies the values to 37.76 and 32.43 at $T = 280$ K and 300 K, respectively, in much better agreement with the experimental results. Alternatively, ϵ_r was also calculated using the PE (employed on the QC calculations) in order to evaluate how the model performs in predicting the dipole moment surface, which might affect the NLO responses. The induced dipole moments were calculated using the CPPE (C++ and Python library for PE) library,[57] and they lead to values about 10% larger than those with

the non-polarizable OPLS-AA but remain still smaller than the experimental results, i.e., $\epsilon_r = 25.74$ (OPLS-AA) and $\epsilon_r = 27.81$ (PE) for $T = 300$ K.

3.1.2 MeOH–air interface. The density profile of the MeOH slabs shows the expected decrease of the density with the temperature, with ρ_{center} values being smaller than the corresponding values from the bulk MD simulations by a maximum of 0.006 g cm^{-3} (Fig. 3 and Table 2). The D values increase with the temperature, from 2.37 Å to 2.99 Å, because the higher the temperature the larger the kinetic energy and, consequently, the larger the roughness, enlarging the region (i.e., the average value of the thickness) where the density changes from 90% to 10%. This value is slightly smaller than those obtained by Matsumoto and Kataoka[58,59] (~ 3.4 Å). Complementary, the density profiles of the first four molecular layers were evaluated and fitted using Gaussian functions. The densities of the first layer (L$_1$) peak at 2.40 Å, 2.49 Å, and 2.59 Å below the interface with 0.591 g cm^{-3}, 0.547 g cm^{-3}, and 0.513 g cm^{-3} values for $T = 260$ K, 280 K, and 300 K, respectively. Going to deeper layers, the density peaks shift by 4.51 Å, 4.71 Å, and 4.93 Å for the T value given in the same order, indicating thicker layers. Note that these values are also larger than the ~ 2.7 Å shifts observed in water MD simulations.[20] This behavior is confirmed with the increase of the half-width at half-maximum (HWHM) values of the Gaussians with the temperature. Notably, the peak densities for the second to fourth molecular layers are similar, indicating a fast convergence to the bulk structure.

The average numbers of H-bonds of MeOH were evaluated separately for the intralayer and interlayer contributions (Table 3). The number of intralayer H-bonds for the molecules belonging to L$_1$ is around 1.25, which is larger than the corresponding intralayer values for deeper layers (~ 0.9). These results indicate strong intralayer interactions at the topmost layer and suggest that L$_1$ is ordered in a 2D-like network, as observed for the water interface.[60] Moreover, the interlayer values are around 0.5, with slightly larger values between L$_1$ and L$_2$ because of the trend of each MeOH molecule to form almost 2 H-bonds and because the first layer interacts only with the second one. This trend is the same for the three temperatures. Yet, all these values decrease in a consistent way at higher
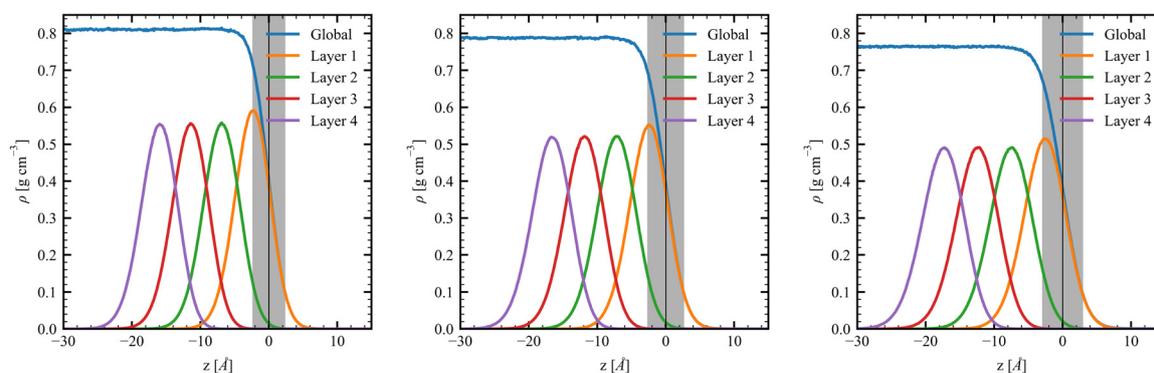

Fig. 3 Interfacial density profiles for the MeOH slabs at (left) $T = 260$ K, (center) $T = 280$ K, and (right) $T = 300$ K, as well as for its first four layers. The interfacial position (black vertical line) and interfacial roughness (gray shade) are also presented.

8662 | *Phys. Chem. Chem. Phys.*, 2024, **26**, 8658–8669

This journal is © the Owner Societies 2024

Table 2 Structural properties of MeOH slab as a function of the temperature extracted using eqn (12). The peak density, peak position, and half-width at half-maximum (HWHM) were obtained by fitting Gaussian functions

Temperature	260 K	280 K	300 K
ρ_{center} [g cm^{-3}]	0.811	0.788	0.765
D [Å]	2.37	2.66	2.99
Peak density [g cm^{-3}]			
L$_1$	0.591	0.547	0.513
L$_2$	0.554	0.520	0.489
L$_3$	0.556	0.521	0.489
L$_4$	0.551	0.520	0.489
Peak shift [Å]			
L$_1$	2.40	2.49	2.59
L$_2$	6.91	7.20	7.52
L$_3$	11.45	11.94	12.48
L$_4$	15.99	16.67	17.43
HWHM [Å]			
L$_1$	3.03	3.30	3.58
L$_2$	3.14	3.38	3.65
L$_3$	3.12	3.36	3.62
L$_4$	3.12	3.37	3.63

Table 3 Average numbers of H-bonds as a function of the layer (L$_i$) and temperature. The total value corresponds to the L$_{i-1,i}$ + L$_{i,i}$ + L$_{i,i+1}$ sum

i	L$_{i,i}$	L$_{i,i+1}$	Total
T = 260 K			
1	1.29	0.54	1.83
2	0.90	0.50	1.94
3	0.90	0.48	1.88
T = 280 K			
1	1.25	0.51	1.76
2	0.89	0.46	1.86
3	0.90	0.46	1.81
T = 300 K			
1	1.21	0.47	1.68
2	0.86	0.45	1.78
3	0.88	0.45	1.77

temperatures, following the density evolution. Furthermore, the average values for the total number of H-bonds, encompassing both the intralayer and interlayer ones, are like those obtained in the bulk MD simulations already for L$_2$. Thus, from the structural point of view, only L$_1$ is distinguishable from the bulk, and therefore, one can assume it is the dominant contribution to the interfacial SHG responses.

3.2 Linear and nonlinear optical responses

3.2.1 Bulk MeOH. The linear and nonlinear optical properties were evaluated for one MeOH molecule embedded in a PE environment encompassing all the surrounding molecules whose center-of-mass is inside a sphere of radius R ranging from 15 Å to 30 Å. Moreover, a mixed embedding including polarizable sites up to 20 Å and an extra shell of point charges up to 30 Å was also tested. The results for T = 300 K are very similar for all R values (Table S1, ESI†), indicating that the optical properties are already converged when including the surrounding molecules within a sphere of 20 Å radius as approximated by one shell of polarizable and point charge

sites, and that an extra shell of point charges does not affect the result. This is in line with a reported non-negligible influence on the NLO responses of molecular switches due to the electrostatic effects of point charges up to ∼25 Å in acetonitrile solution.[61] Moreover, the extra shell of point charges does not impact the probed properties, indicating that the missing polarization at the cutoff border has weak or negligible effects on the probed MeOH molecules. In summary, the $\langle\alpha\rangle$ values amount to about 20 a.u., while $\Delta\alpha \sim$ 6 a.u., and $\beta_{HRS} \sim$ 26 a.u. with a DR of 4.4. Yet, the values of the vectorial components of β are between 0.8 a.u. and 4.2 a.u. with large standard deviations (∼35 a.u.), confirming that it vanishes in the bulk region, as expected for an isotropic medium (Fig. S4, ESI†).

Additionally, for R = 15 Å and 20 Å, the linear and nonlinear properties were also probed at different temperatures to ensure convergence in these thermodynamic conditions. This assessment of the model was realized because the number of MeOH molecules is larger in denser regions (at lower T) and, therefore, may induce stronger interactions. Like T = 300 K, the results are very similar for R = 15 Å and 20 Å at the different temperatures (Table S2, ESI†). In addition, though $\langle\alpha\rangle$ and β_{HRS} hardly change with T, a smooth increase with the temperature is observed for $\beta_{\parallel}$ and DR. The variation in $\beta_{\parallel}$ are attributed to those in $\theta_{(\mu,\beta)}$. Owing to the similarity of results obtained with different embedding sizes (at different T), all the following NLO results are obtained with R = 20 Å. In fact, surrounding molecules are included provided that the position of their center-of-mass is less than 20 Å away from the center-of-mass of the central MeOH molecule. Since the QC part includes up to 6 molecules, this criterium ensures at least 15 Å embedding for each MeOH molecule. These results are presented in Table 4. In addition, Table S3 (ESI†) contains the linear and nonlinear optical properties obtained at different temperatures as a function of the number N of MeOH molecules in the QC region. For the examined properties, the reported values were obtained by dividing the total values by the number of MeOH molecules in the QC region.

$\langle\alpha\rangle$ is weakly impacted by both the temperature and the number of QC molecules (Table 4 and Table S3, ESI†). It amounts to about 20.3 a.u. with differences smaller than 0.2 a.u. and a slight tendency to larger values at higher

Table 4 Temperature effects on the MeOH bulk linear and nonlinear optical properties as obtained using a 20 Å radius embedding. The quantum region comprises one MeOH molecule (N = 1). All results are in atomic units, except $\theta_{(\mu,\beta)}$ (°) and DR (dimensionless)

Property	T = 260 K	T = 280 K	T = 300 K
$\langle\alpha\rangle$	20.39 ± 0.36	20.37 ± 0.39	20.37 ± 0.43
$\Delta\alpha$	5.69 ± 1.94	6.67 ± 1.92	6.08 ± 1.80
$\lvert\vec{\mu}\rvert$	0.98 ± 0.08	0.95 ± 0.10	0.95 ± 0.10
$\beta_{\parallel}$	−12.26 ± 9.26	−13.88 ± 9.61	−14.54 ± 9.84
$\theta_{(\mu,\beta)}$	109.95 ± 14.49	113.26 ± 14.98	113.57 ± 14.96
β_{HRS}	26.73 ± 5.05	26.27 ± 4.94	26.59 ± 5.40
DR	4.25 ± 1.06	4.38 ± 1.15	4.43 ± 1.19
β_x	−6.86 ± 36.56	5.06 ± 34.21	4.12 ± 36.97
β_y	−0.86 ± 34.54	−0.33 ± 35.24	2.87 ± 34.97
β_z	7.15 ± 33.94	−1.98 ± 35.84	1.00 ± 35.04

temperatures. Contrarily, increasing N induces a decrease in $\Delta\alpha$ (per molecule) from ~ 6 a.u. for $N = 1$ to ~ 2.5 a.u. for $N = 6$, indicating that the larger the cluster the more isotropic the response. Additionally, $\Delta\alpha$ is systematically smaller at $T = 260$ K. The magnitude of the dipole moment is also very similar over the range of temperatures, and it decreases with N by a factor of 2. On the NLO side, the $\vec{\beta}$ values ($\beta_\parallel$ as well as its components) are oscillating around zero with large standard deviations, indicating its disappearance for a complete statistical sampling of an isotropic environment. Then, the β_{HRS} values decrease with N (from 26 to 13, and to 10 a.u.), which suggests a fast convergence with N. Yet, slight variations with the temperature are observed. The DR ~ 4.0–4.4 values indicate that the MeOH molecules closely behave like a 1-D harmonophore. In the case of $\beta_\parallel$ no clear trend is observed when increasing T, except for $N = 1$ when the $\beta_\parallel$ amplitude clearly increases with T. Experimentally, Campo *et al.*[62] reported a β_{HRS} value ~ 12 a.u. at $\lambda = 1072$ nm for methanol solution at room temperature (using 1 a.u. $= 8.639 \times 10^{-33}$ esu and $\beta_{HRS} = \sqrt{6/35}\beta_{zzz}^{eff}$). This fair agreement using the $N = 1$ model may be related to the fair description of the long-range interactions dictated by the dipole moment surface and the dielectric constant and mainly to the fair description of the short-range interactions associated with the hydrogen bonding molecules created by the PE model. This agreement becomes more accurate when considering more MeOH molecules in the QC region. Therefore, a systematic study of the dipole moment surface of different solutions and its effects on the NLO properties should clarify whether the scattering units are individual molecules or clusters of molecules.

3.2.2 MeOH–air interface. The linear and nonlinear properties of the MeOH–air interface were then probed, also by considering different embedding sizes ($T = 300$ K and $N = 1$, Table S4, ESI†). In these analyses, the QC region consists of one MeOH molecule of the first layer. The $\langle\alpha\rangle$ values are around 21 a.u. with small standard deviations (~ 0.5 a.u.), contrarily to the small increase of $\Delta\alpha$ from 7.97 a.u. (for $R = 15$ Å) to 8.18 a.u. (for $R = 30$ Å) with standard deviations being 30% of the average values. Like the bulk properties, in the probed radius range, the embedding size has no impact on $|\vec{\mu}|$ and a minimal effect on $\theta_{(\mu,\beta)}$ (a decrease of 0.7°). Nevertheless, a decrease of $\sim 5\%$ is observed on the $\beta_\parallel$ amplitude. These embedding effects are even smaller on β_{HRS} and DR, where the average values change by less than 1% and 3%, respectively. The vectorial β_x and β_y values are oscillating around zero with large standard deviations, which contrasts with the distinct nonzero value of β_z, characteristic of the interfacial symmetry. In summary, the results (Table S4, ESI†) are independent of the choice of the R values, and a sphere of radius 20 Å is also used on the following calculations to ensure at least 15 Å embedding for each MeOH molecule.

Splitting the interfacial region into molecular layers allows for understanding on how the molecular property depends on its interfacial or bulk character. It also provides an evolution of the properties when going from L_1 to L_4. The data are presented in Table 5 for L_1 and Tables S5–S7 (ESI†) for L_2–L_4, and in Fig. 4 and Fig. S5–S7 (ESI†). In general, the $\langle\alpha\rangle$ values decrease ($\sim 2\%$)

Table 5 Linear and nonlinear optical properties of MeOH molecules in L_1 obtained at different temperatures as a function of the number of MeOH molecules in the quantum region. All results are in atomic units, except $\theta_{(\mu,\beta)}$ (°) and DR (dimensionless). μ, α, and β quantities are given per MeOH molecule

Property	$T = 260$ K	$T = 280$ K	$T = 300$ K
$N = 1$			
$\langle\alpha\rangle$	20.75 ± 0.42	20.71 ± 0.49	20.77 ± 0.53
$\Delta\alpha$	9.96 ± 2.51	9.36 ± 2.71	8.72 ± 2.78
$|\vec{\mu}|$	0.94 ± 0.10	0.94 ± 0.09	0.91 ± 0.10
$\beta_\parallel$	-13.08 ± 9.66	-14.21 ± 9.46	-16.06 ± 10.70
$\theta_{(\mu,\beta)}$	109.54 ± 14.50	112.89 ± 15.34	113.32 ± 14.79
β_{HRS}	29.24 ± 5.93	27.92 ± 5.59	30.26 ± 6.15
DR	4.29 ± 1.15	4.39 ± 1.35	4.48 ± 1.17
β_x	-1.53 ± 40.55	-6.12 ± 38.06	7.45 ± 36.73
β_y	-6.40 ± 41.19	-1.68 ± 39.44	1.57 ± 43.72
β_z	-17.98 ± 29.64	-14.37 ± 30.69	-19.55 ± 36.79
$N = 3$			
$\langle\alpha\rangle$	20.61 ± 0.27	20.64 ± 0.27	20.73 ± 0.28
$\Delta\alpha$	6.48 ± 2.18	6.40 ± 2.04	5.68 ± 1.96
$|\vec{\mu}|$	0.67 ± 0.20	0.61 ± 0.21	0.59 ± 0.20
$\beta_\parallel$	-1.86 ± 10.38	0.23 ± 11.32	0.53 ± 10.33
$\theta_{(\mu,\beta)}$	94.68 ± 30.79	87.21 ± 34.45	86.94 ± 34.12
β_{HRS}	15.95 ± 4.34	15.64 ± 3.96	15.41 ± 4.10
DR	4.54 ± 1.57	4.41 ± 1.45	4.16 ± 1.53
β_x	1.08 ± 20.37	-2.71 ± 21.98	1.15 ± 19.80
β_y	-2.35 ± 22.23	0.61 ± 18.92	-2.14 ± 20.92
β_z	-16.84 ± 17.83	-16.16 ± 17.42	-13.96 ± 16.70
$N = 6$			
$\langle\alpha\rangle$	20.61 ± 0.19	20.66 ± 0.22	20.73 ± 0.22
$\Delta\alpha$	4.82 ± 1.48	5.01 ± 1.54	4.49 ± 1.58
$|\vec{\mu}|$	0.46 ± 0.17	0.43 ± 0.16	0.41 ± 0.15
$\beta_\parallel$	-2.26 ± 9.25	-1.68 ± 8.69	-2.07 ± 8.05
$\theta_{(\mu,\beta)}$	97.17 ± 33.48	94.56 ± 34.25	97.90 ± 30.78
β_{HRS}	12.31 ± 3.49	11.96 ± 3.41	11.91 ± 3.34
DR	4.83 ± 1.46	4.66 ± 1.54	4.77 ± 1.44
β_x	-0.81 ± 15.06	-2.22 ± 15.72	-1.98 ± 14.81
β_y	0.03 ± 15.46	-0.09 ± 12.79	-1.93 ± 16.63
β_z	-17.83 ± 13.14	-16.97 ± 13.25	-14.54 ± 12.76

toward the bulk reference value (~ 20.3 a.u.) and present a very small increase with T. Yet, increasing N does not affect its values (*i.e.*, its value per MeOH molecule). Similarly, from L_1 to L_4, $\Delta\alpha$ decreases by a 1.3–1.8 factor towards the bulk value (~ 3 a.u. for $N = 6$). Increasing N leads to more isotropic (QC) clusters, therefore strongly affecting $\Delta\alpha$, *i.e.*, a decrease from 8.72 a.u. ($N = 1$) to 5.68 a.u. ($N = 3$), and to 4.49 a.u. ($N = 6$) for L_1 at $T = 300$ K.

On the other hand, no clear trends can be drawn for $|\vec{\mu}|$ and $\theta_{(\mu,\beta)}$ as a function of the molecular layer, even though $|\vec{\mu}|$ decreases at higher temperatures and for larger N (due to the increased isotropicity of the QC region). $|\vec{\mu}|$ is almost constant, within 10%, as a function of the layer. Then, $\theta_{(\mu,\beta)}$ approaches 90° for $N = 3$ and 6, which is consistent with the decrease of $\beta_\parallel$ ($\cos\theta_{(\mu,\beta)}$ tends to zero). Moreover, the $\beta_\parallel$ values slightly oscillate from L_1 to L_4 and show an increase with T from L_1 to L_2. These small variations on $\beta_\parallel$ as a function of the molecular layer go in opposite directions to the strong effects on β_z in L_1 (Fig. 4) because the dipole moment is preferentially oriented in the interfacial plane (perpendicular to the Z-direction). In general, the first hyperpolarizability vector is strongly affected by the symmetry and the molecular distributions, leading to
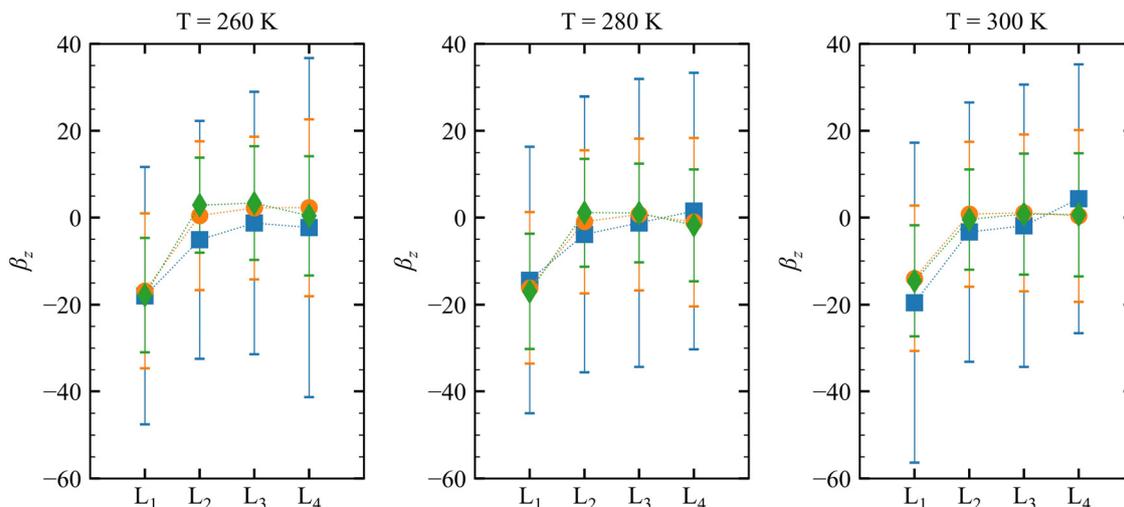
8664 | *Phys. Chem. Chem. Phys.*, 2024, **26**, 8658–8669

This journal is © the Owner Societies 2024

Fig. 4 β_z values, as a function of the molecular layer, calculated at $\lambda = 1064$ nm. The average values (per molecule) are represented by symbols (blue squares for $N = 1$, orange circles for $N = 3$, and green diamonds for $N = 6$), whereas the standard deviations are given by error bars.

large standard deviations. However, the standard error of the mean (SEM) associated to 100 sampled configurations amounts to 0.1 of the respective standard deviation (STD), allowing direct comparisons between the results. (SEM $= \text{STD}/\sqrt{N_{\text{sampled}}}$, where $N_{\text{sampled}} = 100$ is the number of sampled configurations in the QC calculations). The results obtained for β_{HRS} show a small decrease as a function of the molecular layer and with N, but no direct relationship with the temperature. Moreover, all values are within the standard deviation error, indicating no distinction among the molecular layers. Analogously to $\beta_{\parallel}$, the β_{HRS} response is also not selective to the interface but for different reasons. The β_{HRS} is originally used to evaluate the first hyperpolarizability of molecules in gas phase or in solution, where they present random orientations. This is not the case at the interface due to the preferential orientation of the molecules. However, the β_{HRS} values are reported as a matter of comparison with the bulk values to help understanding the convergence of the molecular orientational average.

Table 6 collects the β_{ZZZ}, β_{ZXX}, and β_{XZX} values as a function of N and of L_i for $T = 260$ K, whereas those for $T = 260$ K and 280 K are in Tables S8 and S9 (ESI†). The β_{ZZZ} values of the first molecular layer are clearly distinct from the others with a small decrease between $N = 1$ and $N = 6$, and it dominates β with values one order of magnitude larger than β_{ZXX} and β_{XZX}. Increasing N (from 1 to 6) narrows the data distribution and drives the values toward zero for L_2–L_4. These results also satisfy the Kleinman's rule for $N = 1$ and $N = 6$, where $\beta_{ZXX} = \beta_{XZX}$ far away from resonances.[63] The projections onto the Z axis of the OH and CO bonds were computed for the $N = 1$ model at L_1 to investigate the correlation between the β_{ZZZ} response and the MeOH orientation. Positive values of the projection indicate that the bond points upward [H of OH (O of CO) pointing towards increasing Z projection] and negative downward. About 70% of configurations present at least one of the two bonds pointing towards the bulk, while 50% present both bonds pointing downward. On the other hand, only 13%

Table 6 β tensor components (per MeOH molecule) of the first layers as given in the laboratory frame, together with their corresponding $\chi^{(2)}$ components for the first layer. The results were obtained for $N = 1$, 6, and 1(6) [see text for details of $N = 1(6)$]. All of them were obtained at $T = 300$ K and are in atomic units unless explicitly stated

Property	$N = 1$	$N = 6$	$N = 1(6)$
L_1			
β_{ZZZ}	-17.78 ± 25.48	-12.64 ± 8.80	-31.14 ± 71.90
β_{ZXX}	-2.00 ± 12.35	-1.21 ± 4.20	-7.52 ± 109.54
β_{XZX}	-1.98 ± 12.39	-1.21 ± 4.22	-4.72 ± 20.67
L_2			
β_{ZZZ}	-2.03 ± 17.31	0.67 ± 6.84	-5.03 ± 67.87
β_{ZXX}	-0.98 ± 14.36	-0.35 ± 4.74	17.13 ± 98.38
β_{XZX}	-0.97 ± 14.40	-0.35 ± 4.74	-7.42 ± 19.47
L_3			
β_{ZZZ}	0.17 ± 17.88	1.89 ± 8.98	0.21 ± 68.21
β_{ZXX}	-1.09 ± 12.37	-0.64 ± 4.34	-6.06 ± 90.07
β_{XZX}	-1.09 ± 12.39	-0.65 ± 4.35	-8.28 ± 17.61
L_4			
β_{ZZZ}	2.35 ± 19.10	1.09 ± 9.93	-22.31 ± 71.65
β_{ZXX}	0.37 ± 11.45	-0.78 ± 4.33	-0.25 ± 90.74
β_{XZX}	0.37 ± 11.47	-0.79 ± 4.34	-8.20 ± 17.50
L_1			
$\chi^{(2)}_{ZZZ}$	-7.27 ± 10.42	-5.17 ± 3.60	-12.73 ± 29.39
$\chi^{(2)}_{ZXX}$	-0.82 ± 5.05	-0.49 ± 1.72	-3.08 ± 44.78
$\chi^{(2)}_{XZX}$	-0.81 ± 5.07	-0.49 ± 1.73	-1.93 ± 8.45
$L_1 - \chi^{(2)}$ values given in pm V^{-1}			
$\chi^{(2)}_{ZZZ}$	-14.14 ± 20.26	-10.06 ± 7.00	-24.77 ± 57.19
$\chi^{(2)}_{ZXX}$	-1.59 ± 9.82	-0.96 ± 3.34	-5.98 ± 87.12
$\chi^{(2)}_{XZX}$	-1.57 ± 9.86	-0.96 ± 3.36	-3.75 ± 16.44

of the snapshots present both bonds pointing upward. More importantly, Fig. 5 shows that the β_{ZZZ} response follows the CO bond Z-orientation, and that negative β_{ZZZ} values originate from this preferential downward MeOH orientation.

Then, the results obtained with $N = 6$ were decomposed to disentangle the individual contributions of the central MeOH molecule. These results, referred to as $N = 1(6)$, lead to different conclusions. First, the data distributions are much broader,
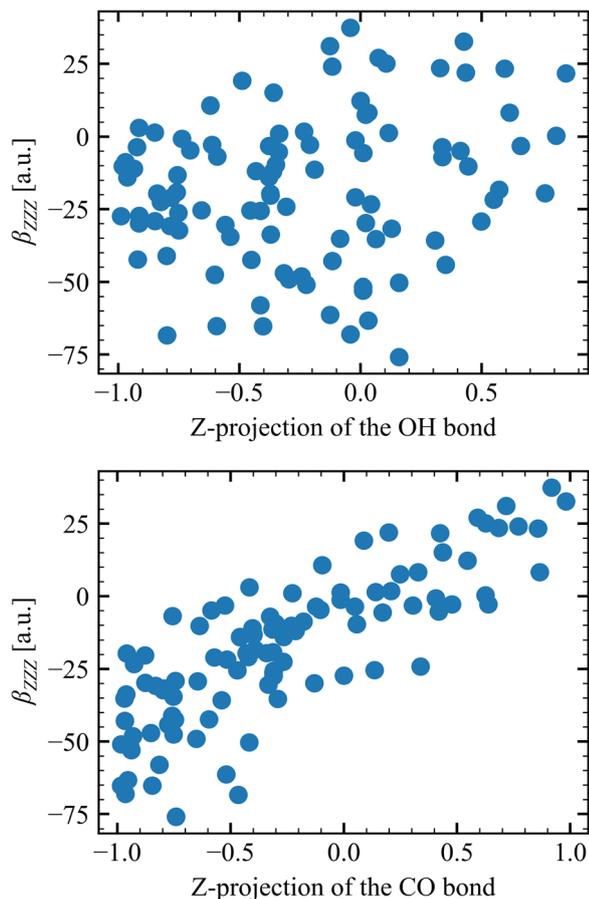
This journal is © the Owner Societies 2024

Phys. Chem. Chem. Phys., 2024, **26**, 8658–8669 | **8665**

Fig. 5 Correlation between the β_{ZZZ} response and the orientation of the OH (top) and CO (bottom) bond, as determined by their projections onto the Z axis.

and the components are no longer specific to the interface. Indeed, by using the LoProp decomposition scheme, the trend of the components to become zero when going deeper and deeper toward the bulk is lost with average values larger than 5 a.u. and standard deviations up to 110 units. Moreover, β_{ZZZ} is not vanishing at L_4, neither β_{ZXX} at L_2. Furthermore, Kleinman's rule is also violated. These results evidently indicate that the decomposition scheme is not suitable for this study case and that it should be modified. This deficiency may be related to the number N of close MeOH molecules because it induces asymmetries in the individual contributions, and including the second solvation shell may improve the accuracy.

The same trends are observed for $T = 260$ K and 280 K, and no clear relationship can be drawn as a function of the temperature due to the large values of the standard deviations.

At the macroscopic scale, the optical responses are expressed as a power series of the polarization [B convention, eqn (13)] where the $\chi^{(n)}$ is the nth order susceptibility tensor. Comparing eqn (13) with (1), a relationship between the macroscopic and microscopic responses is drawn [eqn (14)]. This relationship depends on the density of particles ($\rho_N = \rho N_A / MM$, where ρ is the mass density, MM the molar mass, and N_A the Avogadro's number) and on the orientational average of the

β tensor ($\langle\beta\rangle_{OR}$). ϵ_0 is the vacuum electric permittivity.

$$P_i(\omega_\sigma) = \epsilon_0 \left(\sum_j \chi_{ij}^{(1)} E_j^{\omega_1} + \sum_{j,k} \chi_{ijk}^{(2)} E_j^{\omega_1} E_k^{\omega_2} + \sum_{j,k,l} \chi_{ijkl}^{(3)} E_j^{\omega_1} E_k^{\omega_2} E_l^{\omega_3} + \cdots \right),$$

(13)

$$\chi^{(2)} = \frac{1}{2\epsilon_0} \rho_N \langle\beta\rangle_{OR}$$

(14)

The second-order susceptibility $[\chi^{(2)}(-2\omega;\omega,\omega)]$ probed in surface-SHG experiments is reduced to only three non-vanishing tensor elements ($\chi_{ZZZ}^{(2)}$, $\chi_{ZXX}^{(2)}$, and $\chi_{XZX}^{(2)}$) because the air–liquid interface symmetry leads to rotational invariants about the surface normal direction.[23] On the one hand, $\langle\beta_{OR}\rangle$ is well-defined and broadly used for predicting the orientation of adsorbed molecules on surfaces.[3,4,8,64] On the other hand, performing this orientational average for liquid–air interfaces and then obtaining the microscopic–macroscopic ($\beta - \chi^{(2)}$) relationship is still not fully established.[19] Indeed, contributions different from those of the $\Delta\vec{\mu}(\omega_\sigma)$ expansion might also affect the experimental measurements, e.g., the bulk quadrupole contributes for systems with weak interfacial dipolar signals.[65]

Looking for the macroscopic dipolar responses, the $\chi^{(2)}$ values were estimated by multiplying the corresponding average β_{ZZZ}, β_{ZXX}, and β_{XZX} components with the number density associated with the first molecular layer (Table 2). This is a reliable approximation because the average β values encompass the orientational averaging over the extracted snapshots and only the first molecular layer presents net β responses. At $T = 300$ K, the corresponding number density is $\rho_N = 6.51 \times 10^{-2}$ particles bohr^{-3}. The $\chi^{(2)}$ values of L_1 are given at the bottom of Table 6 for experimental comparison purpose.

Experimentally, the $\chi_{ZZZ}^{(2)}/\chi_{ZXX}^{(2)}$ ratio is often reported, and the corresponding β_{ZZZ}/β_{ZXX} quantities are plotted in Fig. 6 for the successive layers and for different QC schemes. Both $N = 1$ and
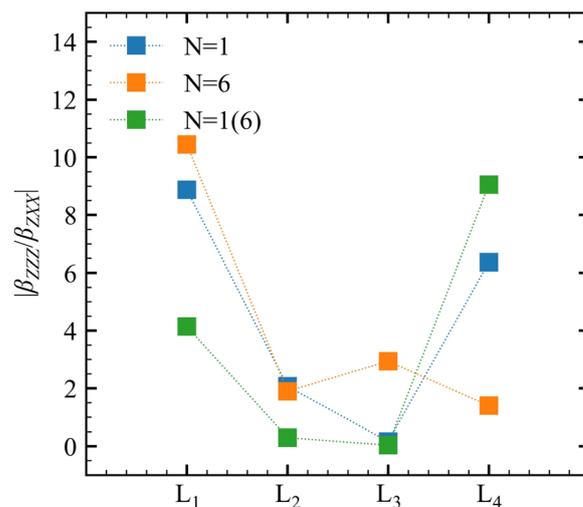

Fig. 6 $|\beta_{ZZZ}/\beta_{ZXX}|$ ratio as a function of the molecular layer obtained at $T = 300$ K for different QC schemes. Note that the value obtained for $N = 1(6)$ at L_4 is divided by 10 for clarity.

8666 | *Phys. Chem. Chem. Phys.*, 2024, **26**, 8658–8669

This journal is © the Owner Societies 2024

$N = 6$ models predict large ratios (~ 10) at the interface with a net decrease towards the bulk (~ 2). The obtained values are comparable with the $\chi_{ZZZ}^{(2)}/\chi_{ZXX}^{(2)}$ ratios (around 5) reported for longer alcohols ranging from butanol to undecanol.[23] Using $N = 1$, an unexpectedly large value is observed for L_4. It is ascribed to the large statistical fluctuations of these properties (between 10 and 20 a.u.). The ratios obtained using the $N = 1(6)$ model are smaller than those obtained with $N = 1$ and $N = 6$, except for L_4, which achieves a value of about 90 and is not reliable.

4. Conclusions

The second harmonic generation (SHG) responses of the methanol–air interface have been evaluated by adopting a sequential method, classical molecular dynamics (MD) then quantum chemistry (QC). This approach ensures the configurational diversity required to subsequently evaluate the average values of the first hyperpolarizability, which is a dynamical and symmetry-dependent property. Additionally, temperature effects on the linear and nonlinear optical responses have been studied. Within this approach, the molecular properties were disentangled as a function of molecular layers to which the MeOH molecules belong while different numbers of MeOH molecules were treated at the QC level. The main results are (i) the mean polarizability $\langle \alpha \rangle$ is almost insensitive to the interface, with values about 2% larger than those obtained in bulk, (ii) conversely, a smooth decrease is observed in the polarizability anisotropy $\Delta\alpha$, indicating a linear optical interface thickness of around 20 Å, corresponding to 4 MeOH molecular layers, (iii) for the molecular SHG responses, $\beta(-2\omega;\omega,\omega)$, the interfacial dependence is strong and limited to the first molecular layer (~ 3.0 Å). This narrow interface is characterized by a high contrast in the β_{ZZZ} tensor component between the first (non-null values) and the subsequent (values toward zero) layers. Moreover, the average β_{ZXX} and β_{XZX} values satisfy the Kleinman's symmetry rule within the dipolar molecular responses. Therefore, the model including six MeOH molecules (a central molecule plus its five nearest neighbors) in the QC region performs the best in capturing the SHG response of the methanol–air interface and its progression toward the bulk values. Furthermore, similar trends are obtained at different temperatures or when increasing the number of MeOH molecules treated at the QC level, which indicates the robustness of the employed approach for describing the dipolar molecular responses of air–liquid interfaces.

Conflicts of interest

The authors declare no competing financial interest.

Acknowledgements

References

1 J. Zhong, M. Kumar, J. Anglada, M. Martins-Costa, M. Ruiz-Lopez, X. Zeng and J. S. Francisco, Atmospheric spectroscopy and photochemistry at environmental water interfaces, *Annu. Rev. Phys. Chem.*, 2019, **70**, 45–69.

2 M. F. Ruiz-Lopez, J. S. Francisco, M. T. C. Martins-Costa and J. M. Anglada, Molecular reactions at aqueous interfaces, *Nat. Rev. Chem.*, 2020, **4**, 459–475.

3 Y. R. Shen, Surface properties probed by second-harmonic and sum-frequency generation, *Nature*, 1989, **337**, 519–525.

4 Y. Shen, Optical second harmonic generation at interfaces, *Annu. Rev. Phys. Chem.*, 1989, **40**, 327–350.

5 N. Bloembergen and P. S. Pershan, Light waves at the boundary of nonlinear media, *Phys. Rev.*, 1962, **128**, 606–622.

6 P. A. Franken, A. E. Hill, C. W. Peters and G. Weinreich, Generation of optical harmonics, *Phys. Rev. Lett.*, 1961, **7**, 118–119.

7 R. J. Tran, K. L. Sly and J. C. Conboy, Applications of surface second harmonic generation in biological sensing, *Annu. Rev. Anal. Chem.*, 2017, **10**, 387–414.

8 K. B. Eisenthal, Liquid interfaces probed by second-harmonic and sum-frequency spectroscopy, *Chem. Rev.*, 1996, **96**, 1343–1360.

9 A. C. McGeachy, E. R. Caudill, D. Liang, Q. Cui, J. A. Pedersen and F. M. Geiger, Counting charges on membrane-bound peptides, *Chem. Sci.*, 2018, **9**, 4285–4298.

10 R. Costa, C. M. Pereira, A. F. Silva, P.-F. Brevet and E. Benichou, Ordering and nonideality of air−ionic liquid interfaces in surface second harmonic generation, *J. Phys. Chem. B*, 2020, **124**, 3954–3961.

11 G. C. Gschwend, A. Olaya and H. H. Girault, How to polarise an interface with ions: the discrete Helmholtz model, *Chem. Sci.*, 2020, **11**, 10807–10813.

12 F. Castet, C. Tonnelé, L. Muccioli and B. Champagne, Predicting the second-order nonlinear optical responses of organic materials: the role of dynamics, *Acc. Chem. Res.*, 2022, **55**, 3716–3726.

13 N. A. Murugan, R. Apostolov, Z. Rinkevicius, J. Kongsted, E. Lindahl and H. Ågren, Association dynamics and linear and nonlinear optical properties of an *n*-acetylaladanamide probe in a POPC membrane, *J. Am. Chem. Soc.*, 2013, **135**, 13590–13597.

14 C. Bouquiaux, F. Castet and B. Champagne, Influence of the nature of the lipid building blocks on the second-order

This journal is © the Owner Societies 2024

Phys. Chem. Chem. Phys., 2024, **26**, 8658–8669 | **8667**

nonlinear optical responses of an embedded di-8-ANEPPS probe, *J. Phys. Chem. B*, 2023, **127**, 528–541.

15 C. Wang, D. Liu and W. Lin, Metal–organic frameworks as a tunable platform for designing functional molecular materials, *J. Am. Chem. Soc.*, 2013, **135**, 13222–13234.

16 C. Tonnelé, B. Champagne, L. Muccioli and F. Castet, Nonlinear optical contrast in azobenzene-based self-assembled monolayers, *Chem. Mater.*, 2019, **31**, 6759–6769.

17 T. T. Pham, A. Jonchère, J.-F. Dufrêche, P.-F. Brevet and O. Diat, Analysis of the second harmonic generation signal from a liquid/air and liquid/liquid interface, *J. Chem. Phys.*, 2017, **146**, 144701.

18 Y. Foucaud, B. Siboulet, M. Duvail, A. Jonchere, O. Diat, R. Vuilleumier and J.-F. Dufrêche, Deciphering second harmonic generation signals, *Chem. Sci.*, 2021, **12**, 15134–15142.

19 G. Le Breton, O. Bonhomme, P.-F. Brevet, E. Benichou and C. Loison, First hyperpolarizability of water at the air–vapor interface: a QM/MM study questions standard experimental approximations, *Phys. Chem. Chem. Phys.*, 2021, **23**, 24932–24941.

20 T. N. Ramos and B. Champagne, Investigation of the second harmonic generation at the water–vacuum interface by using multi-scale modeling methods, *ChemistryOpen*, 2023, **12**, e202200045.

21 A. A. Tamburello-Luca, P. Hébert, P. F. Brevet and H. H. Girault, Resonant-surface second-harmonic generation studies of phenol derivatives at air/water and hexane/water interfaces, *J. Chem. Soc., Faraday Trans.*, 1996, **92**, 3079–3085.

22 G. Le Breton, O. Bonhomme, E. Benichou and C. Loison, Liquid water: when hyperpolarizability fluctuations boost and reshape the second harmonic scattering intensities, *J. Phys. Chem. Lett.*, 2023, **14**, 4158–4163.

23 R. Antoine, F. Bianchi, P. F. Brevet and H. H. Girault, Studies of water/alcohol and air/alcohol interfaces by second harmonic generation, *J. Chem. Soc., Faraday Trans.*, 1997, **93**, 3833–3838.

24 T. Verbiest, K. Clays and V. Rodriguez, *Second-order Nonlinear Optical Characterization Techniques: An Introduction*, CRC Press, New York, 2009.

25 E. Hendrickx, K. Clays and A. Persoons, Hyper-Rayleigh Scattering in Isotropic Solution, *Acc. Chem. Res.*, 1998, **31**, 675–683.

26 F. Castet, E. Bogdan, A. Plaquet, L. Ducasse, B. Champagne and V. Rodriguez, Reference molecules for nonlinear optics: a joint experimental and theoretical investigation, *J. Chem. Phys.*, 2012, **136**, 024506.

27 W. L. Jorgensen, D. S. Maxwell and J. Tirado-Rives, Development and testing of the OPLS all-atom force field on conformational energetics and properties of organic liquids, *J. Am. Chem. Soc.*, 1996, **118**, 11225–11236.

28 E. E. Roper, The freezing point of methanol; a simple type of cryostat applicable to freezing point determinations, *J. Am. Chem. Soc.*, 1938, **60**, 1693–1695.

29 R. W. Hockney, S. P. Goel and J. W. Eastwood, Quiet high-resolution computer models of a plasma, *J. Comput. Phys.*, 1974, **14**, 148–158.

30 U. Essmann, L. Perera, M. L. Berkowitz, T. Darden, H. Lee and L. G. Pedersen, A smooth particle mesh Ewald method, *J. Chem. Phys.*, 1995, **103**, 8577–8593.

31 G. Bussi, D. Donadio and M. Parrinello, Canonical sampling through velocity rescaling, *J. Chem. Phys.*, 2007, **126**, 014101.

32 H. J. C. Berendsen, J. P. M. Postma, W. F. van Gunsteren, A. DiNola and J. R. Haak, Molecular dynamics with coupling to an external bath, *J. Chem. Phys.*, 1984, **81**, 3684–3690.

33 B. Hess, H. Bekker, H. J. C. Berendsen and J. G. E. M. Fraaije, LINCS: a linear constraint solver for molecular simulations, *J. Comput. Chem.*, 1997, **18**, 1463–1472.

34 H. J. C. Berendsen, D. van der Spoel and R. van Drunen, GROMACS: a message-passing parallel molecular dynamics implementation, *Comput. Phys. Commun.*, 1995, **91**, 43–56.

35 D. van der Spoel, E. Lindahl, B. Hess, G. Groenhof, A. E. Mark and H. J. C. Berendsen, GROMACS: fast, flexible, and free, *J. Comput. Chem.*, 2005, **26**, 1701–1718.

36 W. Humphrey, A. Dalke and K. Schulten, VMD: Visual Molecular Dynamics, *J. Mol. Graphics*, 1996, **14**, 33–38.

37 M. Neumann, Dipole moment fluctuation formulas in computer simulations of polar systems, *Mol. Phys.*, 1983, **50**, 841–858.

38 R. Gowers, M. Linke, J. Barnoud, T. Reddy, M. Melo, S. Seyler, J. Domański, D. Dotson, S. Buchoux, I. Kenney and O. Beckstein, *Proceedings of the 15th Python in Science Conference*, 2016, pp. 98–105.

39 L. B. Pártay, G. Hantal, P. Jedlovszky, Á. Vincze and G. Horvai, A new method for determining the interfacial molecules and characterizing the surface roughness in computer simulations. Application to the liquid–vapor interface of water, *J. Comput. Chem.*, 2008, **29**, 945–956.

40 M. Sega, G. Hantal, B. Fábián and P. Jedlovszky, Pytim: a python package for the interfacial analysis of molecular simulations, *J. Comput. Chem.*, 2018, **39**, 2118–2125.

41 P. Sałek, O. Vahtras, T. Helgaker and H. Ågren, Density-functional theory of linear and nonlinear time-dependent molecular properties, *J. Chem. Phys.*, 2002, **117**, 9630–9645.

42 T. Yanai, D. P. Tew and N. C. Handy, A new hybrid exchange-correlation functional using the Coulomb-attenuating method (CAM-B3LYP), *Chem. Phys. Lett.*, 2004, **393**, 51–57.

43 R. A. Kendall, T. H. Dunning and R. J. Harrison, Electron affinities of the first-row atoms revisited. Systematic basis sets and wave functions, *J. Chem. Phys.*, 1992, **96**, 6796–6806.

44 F. Castet and B. Champagne, Assessment of DFT exchange–correlation functionals for evaluating the multipolar contributions to the quadratic nonlinear optical responses of small reference molecules, *J. Chem. Theory Comput.*, 2012, **8**, 2044–2052.

45 J. M. H. Olsen and J. Kongsted, Molecular properties through polarizable embedding, *Adv. Quantum Chem.*, 2011, **61**, 107–143.

46 N. H. List, H. J. A. Jensen and J. Kongsted, Local electric fields and molecular properties in heterogeneous environments through polarizable embedding, *Phys. Chem. Chem. Phys.*, 2016, **18**, 10070–10080.

8668 | *Phys. Chem. Chem. Phys.*, 2024, **26**, 8658–8669

This journal is © the Owner Societies 2024

47 M. T. P. Beerepoot, A. H. Steindal, N. H. List, J. Kongsted and J. M. H. Olsen, Averaged Solvent Embedding Potential Parameters for Multiscale Modeling of Molecular Properties, *J. Chem. Theory Comput.*, 2016, **12**, 1684–1695.

48 K. Aidas, C. Angeli, K. L. Bak, V. Bakken, R. Bast, L. Boman, O. Christiansen, R. Cimiraglia, S. Coriani, P. Dahle, E. K. Dalskov, U. Ekström, T. Enevoldsen, J. J. Eriksen, P. Ettenhuber, B. Fernández, L. Ferrighi, H. Fliegl, L. Frediani, K. Hald, A. Halkier, C. Hättig, H. Heiberg, T. Helgaker, A. C. Hennum, H. Hettema, E. Hjertenaes, S. Høst, I.-M. Høyvik, M. F. Iozzi, B. Jansík, H. J. A. Jensen, D. Jonsson, P. Jørgensen, J. Kauczor, S. Kirpekar, T. Kjaergaard, W. Klopper, S. Knecht, R. Kobayashi, H. Koch, J. Kongsted, A. Krapp, K. Kristensen, A. Ligabue, O. B. Lutnaes, J. I. Melo, K. V. Mikkelsen, R. H. Myhre, C. Neiss, C. B. Nielsen, P. Norman, J. Olsen, J. M. H. Olsen, A. Osted, M. J. Packer, F. Pawlowski, T. B. Pedersen, P. F. Provasi, S. Reine, Z. Rinkevicius, T. A. Ruden, K. Ruud, V. V. Rybkin, P. Sałek, C. C. M. Samson, A. S. de Merás, T. Saue, S. P. A. Sauer, B. Schimmelpfennig, K. Sneskov, A. H. Steindal, K. O. Sylvester-Hvid, P. R. Taylor, A. M. Teale, E. I. Tellgren, D. P. Tew, A. J. Thorvaldsen, L. Thøgersen, O. Vahtras, M. A. Watson, D. J. D. Wilson, M. Ziolkowski and H. Ågren, *Wiley Interdiscip. Rev.: Comput. Mol. Sci.*, 2014, **4**, 269–284.

49 Dalton, a molecular electronic structure program, Release Dalton2020.1, 2022, see **https://daltonprogram.org**.

50 L. Gagliardi, R. Lindh and G. Karlström, Local properties of quantum chemical systems: the LoProp approach, *J. Chem. Phys.*, 2004, **121**, 4494–4500.

51 O. Vahtras, LoProp for Dalton, 2014, DOI: **10.5281/zenodo.13276**.

52 D. L. Wertz and R. K. Kruh, Reinvestigation of the structures of ethanol and methanol at room temperature, *J. Chem. Phys.*, 1967, **47**, 388–390.

53 K. R. Wilson, R. D. Schaller, D. T. Co, R. J. Saykally, B. S. Rude, T. Catalano and J. D. Bozek, Surface relaxation in liquid water and methanol studied by X-ray absorption spectroscopy, *J. Chem. Phys.*, 2002, **117**, 7738–7744.

54 A. P. Gregory and R. N. Clarke, Traceable measurements of the static permittivity of dielectric reference liquids over the temperature range 5–50 °C, *Meas. Sci. Technol.*, 2005, **16**, 1506–1516.

55 M. Mohsen-Nia, H. Amiri and B. Jazi, Dielectric constants of water, methanol, ethanol, butanol and acetone: measurement and computational study, *J. Solution Chem.*, 2010, **39**, 701–708.

56 M. Jorge and L. Lue, The dielectric constant: Reconciling simulation and experiment, *J. Chem. Phys.*, 2019, **150**, 084108.

57 M. Scheurer, P. Reinholdt, E. R. Kjellgren, J. M. Haugaard Olsen, A. Dreuw and J. Kongsted, CPPE: An open-source C++ and Python library for polarizable embedding, *J. Chem. Theory Comput.*, 2019, **15**, 6154–6163.

58 M. Matsumoto and Y. Kataoka, Molecular orientation near liquid–vapor interface of methanol: Simulational study, *J. Chem. Phys.*, 1989, **90**, 2398–2407.

59 M. Matsumoto and Y. Kataoka, Erratum: Molecular orientation near liquid–vapor interface of methanol [J. Chem. Phys. 90, 2398 (1989)], *J. Chem. Phys.*, 1991, **95**, 7782.

60 S. Pezzotti, A. Serva and M.-P. Gaigeot, 2D-HB-Network at the air–water interface: a structural and dynamical characterization by means of ab initio and classical molecular dynamics simulations, *J. Chem. Phys.*, 2018, **148**, 174701.

61 J. Quertinmont, B. Champagne, F. Castet and M. H. Cardenuto, Explicit versus Implicit Solvation Effects on the First Hyperpolarizability of an Organic Biphotochrome, *J. Phys. Chem. A*, 2015, **119**, 5496–5503.

62 J. Campo, F. Desmet, W. Wenseleers and E. Goovaerts, Highly sensitive setup for tunable wavelength hyper-Rayleigh scattering with parallel detection and calibration data for various solvents, *Opt. Express*, 2009, **17**, 4587–4604.

63 D. A. Kleinman, Nonlinear Dielectric Polarization in Optical Media, *Phys. Rev.*, 1962, **126**, 1977–1979.

64 D. Zimdars and K. B. Eisenthal, Effect of solute orientation on solvation dynamics at the air/water interface, *J. Phys. Chem. A*, 1999, **103**, 10567–10570.

65 S. Sun, J. Schaefer, E. H. G. Backus and M. Bonn, How surface-specific is 2nd-order non-linear spectroscopy?, *J. Chem. Phys.*, 2019, **151**, 230901.

This journal is © the Owner Societies 2024

Phys. Chem. Chem. Phys., 2024, **26**, 8658–8669 | **8669**